Check for updates

Received: 17 December 2023 | Revised: 5 February 2024 | Accepted: 22 February 2024

DOI: 10.1002/ese3.1729

ORIGINAL ARTICLE

Theoretical analysis and numerical study of natural convection inside combined solar chimney

Huimin Cui[1,2,3] | **Mengjiao Han**[4] | **Jitao Zhang**[4] | **Zhiming Han**[1,2,4] | **Feng Xu**[5] | **Qingkuan Liu**[1,2,4]

[1]State Key Laboratory of Mechanical Behavior and System Safety of Traffic Engineering Structures, Shijiazhuang Tiedao University, Shijiazhuang, China

[2]Innovation Center for Wind Engineering and Wind Energy Technology of Hebei Province, Shijiazhuang, China

[3]Department of Mathematics and Physics, Shijiazhuang Tiedao University, Shijiazhuang, China

[4]School of Civil Engineering, Shijiazhuang Tiedao University, Shijiazhuang, China

[5]School of Physical Science and Engineering, Beijing Jiaotong University, Beijing, China

Correspondence
Huimin Cui, and Zhiming Han, State Key Laboratory of Mechanical Behavior and System Safety of Traffic Engineering Structures, Shijiazhuang Tiedao University, Shijiazhuang 050043, China.
Email: huimincui@stdu.edu.cn and hanzm@stdu.edu.cn

Feng Xu, School of Physical Science and Engineering, Beijing Jiaotong University, Beijing 100044, China.
Email: fxu@bjtu.edu.c

Funding information
Central Leading Local Science and Technology Development Fund Project, Grant/Award Number: 236Z5410G; Natural Science Foundation of Hebei Province Innovative Research Group Project, Grant/Award Number: E2022210078; National Natural Science Foundation of China, Grant/Award Number: 11802186; Natural Science Foundation of Hebei Province, Grant/Award Number: E2022210069; High Talents Project of Hebei Province

Abstract

Solar chimneys may induce natural ventilation through solar radiation. However, sufficient theoretical studies are needed as a basis to fully exploit passive design in practical green building design. In this work, we investigate the heat transfer properties of turbulent natural convective flows in a combined solar chimney with a thermal flux at the absorption wall by means of theoretical analysis and numerical simulations. Two different flow patterns have been found, one with a clear thermal boundary layer flow pattern and the other without, based on high Rayleigh numbers. For flow development in these two flow regimes, the transient scaling analysis is performed separately and the control mechanism for each phase is presented. Some new scale relationships are established to characterize the ventilation performance of solar chimneys, including thermal boundary layer thickness δ_T, velocity v_T, mass flow m, and so on. For the distinct thermal boundary layers, $\delta_{T,s} \sim H\Gamma^{2/5}/Bo^{1/5}\kappa^{2/5}$, $v_{T,s} \sim Bo^{2/5}\kappa^{4/5}\Gamma^{1/5}/H$, $m \sim \rho Bo^{1/5}\kappa^{2/5}\Gamma^{3/5}$. For nonobvious thermal boundary layers, $v_{T,f} \sim Bo^{1/3}\kappa/H^{2/3}W^{1/3}$, $m \sim \rho Bo^{1/3}\kappa/A^{2/3}$. The important scale relationships are validated using corresponding numerical simulation data, such as the mass flow rate scale $M \sim (\Gamma/\kappa)^{3/5}Bo^{1/5}$ in the distinct thermal boundary layer flow state, and so on. The air changes per hour and heat exchange efficiencies are calculated for a solar chimney with a fixed height-to-width ratio to provide a basis for the design of a solar chimney.

KEYWORDS
combined solar chimney, heat transfer, natural ventilation, Rayleigh number, scaling analysis, turbulent thermal boundary layer

This is an open access article under the terms of the Creative Commons Attribution License, which permits use, distribution and reproduction in any medium, provided the original work is properly cited.
© 2024 The Authors. *Energy Science & Engineering* published by Society of Chemical Industry and John Wiley & Sons Ltd.

1 | INTRODUCTION

Energy consumption in buildings has been rising every year in response to rapid social development. There has been a lot of interest in finding practical ways to reduce the energy consumption of buildings and enhance their internal thermal environment. An efficient passive design strategy for buildings with zero energy use is to provide natural ventilation using solar chimneys.[1] Miyazaki et al.[2] found that natural ventilation by solar chimneys not only optimizes the indoor environment but also reduces the energy consumption of the building. It can even save 50% of energy per year compared to mechanical ventilation.

Hot pressure ventilation is used in solar chimneys to reduce the consumption of energy. One of the most frequently used sources of renewable energy is solar energy. The study[3] found that buildings using solar chimneys can reduce cooling loads by 30%–100% in summer and heating loads by 46%–56% in winter. Therefore, it is beneficial to use solar chimney enhanced ventilation technology to reduce building energy consumption.

Scaling analysis has been extensively utilized in the past to examine convective flows with various geometries and boundary restrictions. The scale analysis of the transient natural convection in a rectangular side heating cavity with the aspect ratio $A < 1$ shows that under a fixed aspect ratio, the flow is dominated by heat conduction before the Rayleigh number (Ra) exceeds the critical Ra.[4] The numerical simulation and scale analysis of the triangular cavity with inclined wall cooling and underside heating show that the transient phenomenon begins with the cooling of the inclined wall, and there are both hot and sticky layers on the wall.[5,6] Lei and Patterson[7] investigated potential flow patterns caused by solar radiation-induced unsteady natural convection in a small slope triangular cavity. The unsteady natural convection boundary layer of a fluid with $Pr > 1$ was scaled by Lin et al.[8] It was found that the boundary layer's early development was one-dimensional as a result of the influence of pure heat conduction. In the steady state, the development of the boundary layer becomes two-dimensional (2D) as convection dominates. By analyzing the heat transfer characteristics of the upslope flow and the unsteady roof plume in the triangular cavity where periodic heating is applied to the roof, it is found that the development of the upslope flow includes two stages: heat conduction and convection, and the heating time has an impact on the roof flow.[9] For a triangular cavity with linearly increasing temperature applied on the inclined wall, the boundary layer reaches a quasi-steady state before the heating is completed, and the thickness of the thermal boundary layer first increases and then decreases.[10] The scale analysis of the natural convective thermal boundary layer near the suddenly heated inclined plate has obtained the scale relationship between the maximum velocity in the boundary layer, the time when the boundary layer reaches the steady state, the thickness of the thermal layer and the thickness of the viscous layer, and found that the fluid flow state can be divided into three stages: the initial stage, the transition stage and the steady stage.[11] The findings of scale analysis in the above studies[4–11] were verified with numerical results. For solar chimney, He[12] and Rakesh and Lei[13] conducted scaling analysis of laminar natural convection in a vertical solar chimney. It was discovered that the boundary layers in the chimney can be classified into two types: distinct thermal boundary layers and indistinct thermal boundary layers. Thermal boundary layer thicknesses, inner and outer velocity boundary layer thicknesses, and the amount of time required for the boundary layer development to attain a stable state were obtained, representing transient flows. By comparing the results of direct numerical simulations, the accuracy of the dimensional analysis is confirmed.

Numerical simulation and experimentation have been used to study the boundary layer close to the solar chimney's absorption wall. Chen et al.[14] and Li et al.[15] established a rectangular chimney model, laying an electric heating film on a high-density plate and changing the voltage to change the heat flux. Researchers have looked at the temperature and speed characteristics in vertical solar chimney channels of various widths. They found a temperature and velocity boundary layer near the absorber wall of the chimney. The photovoltaic (PV) Trombe wall was numerically simulated using the Renormalization-group (RNG) k–ε model by Lei et al.[16] and Su et al.,[17] and the results showed that a thermal boundary layer exists close to the absorb wall of the chimney. By varying the width of the chimney, the optimal ratio of height to width (aspect ratio) of the chimney is obtained when the ventilation volume achieves its highest value. To characterize the ventilation volume and heat transfer characteristics, the fitting formulas of Nusselt number (Nu) and Reynolds number (Re) as a function of Rayleigh number (Ra) were provided. Imran et al.[18] conducted field tests and 2D numerical simulation studies on the inclined solar chimney model. In the chimney passage, the temperature profiles at various heights along the breadth of the chimney are evaluated. It was found that there is a temperature boundary layer at the absorber wall of the chimney.

In addition, there are other related studies of various types of solar chimneys. Khedari et al.[19] did an

20500505, 2024, 5, Downloaded from https://scijournals.onlinelibrary.wiley.com/doi/10.1002/ese3.1729 by Cochrane France, Wiley Online Library on [05/06/2025]. See the Terms and Conditions (https://onlinelibrary.wiley.com/terms-and-conditions) on Wiley Online Library for rules of use; OA articles are governed by the applicable Creative Commons License

experimental investigation on the rooftop solar chimney, in addition, Zhao,[20] Ramadan Bassiouny and Koura[21] examined the ventilation effect of vertical solar chimney through CFD numerical simulation. All of the findings indicated that when the chimney's aspect ratio rises, the ventilation capacity initially rises and subsequently falls. Xue and Su[22] made an analysis of the flow field characteristics inside the solar chimney by utilizing the computational simulation method, and proposed a gradually shrinking chimney channel structure that can effectively decrease the outlet flow inversion and improve the natural ventilation effect. Vertical solar chimneys were the subject of experimental investigation by Burek and Habeb.[23] Different solar radiation intensities were controlled by using electric heating pads. The ventilation performance under different solar radiation intensity and chimney width was investigated. The quantitative relationship between chimney ventilation rate and solar radiation intensity, and chimney width was obtained. For combined solar chimneys, Yang et al.[24] and Duan[25] studied the influence of different widths, inclined section lengths, and outdoor wind speed on its ventilation performance. It is shown that the ventilation capacity is enhanced as the width and length of the tilt profile increase.

Mandal et al.[26] used artificial neural networks (ANN) to simulate how power generation performance changed under various conditions with regard to solar chimney power generation. They found that reducing the height of the collector inlet and increasing the diameter of the chimney can significantly improve the power generation efficiency, but the cost of increasing the diameter of the chimney is higher. It is discovered that geometric optimization is essential to the efficiency of solar chimney power generation (SCPPs) by examining the experimental procedures and advancements of SCPPs.[27] When the ground sloped absorber ($\gamma = 0.6°$) and divergent chimney ($\phi = +0.75°$), the power generation can be increased by 80%.[28] Stair-shaped absorbers can increase power generation capacity by about 80%.[29] The wave absorber can increase power generation capacity by about 58.61%.[30] Studies conducted on a SCPP indicate that the diameter of the chimney should be 50 cm, and the entrance height should be 7 cm, to reach the highest power generating capacity.[31]

According to earlier research,[32,33] a vertical solar chimney will experience backflow when the chimney width is large. The combined solar chimney combines vertical and inclined solar chimneys. Effectively avoiding outlet backflow and improving ventilation and heat exchange efficiency. In addition, the combination of chimneys and building facades has the advantages of esthetics and a small footprint. Therefore, this study focuses on the combined solar chimney as the research object.

Scale analysis methods have been widely used in the study of natural convective flow and heat transfer,[4–11] but most focus on closed cavities and flat plates. The analysis of transient convection inside a combined solar chimney is still not clear enough. Additionally, because solar radiation and ventilation openings are present, the instantaneous flow and heat transfer characteristics of solar chimney systems are quite complicated. Previous research (such as Tang and colleagues[1,12,13,22]) used steady-state numerical simulation and simple k–ε turbulence models, which are unable to fully represent the instantaneous turbulent flow and heat transfer characteristics in solar chimneys.

Therefore, the combined solar chimney is used in this study as the research object, and scale analysis is used to discuss the development process of the transient flow in the structure. Based on the RNG k–ε turbulence model, the relevant numerical simulation is performed. The control mechanism of each stage of flow development is discussed, and the theoretical relationships of airflow temperature, velocity, and mass flow rate, which characterizes the ventilation performance of the solar chimney, is derived. Air change per hour is used as the evaluation index to demonstrate how applicable solar chimneys are in real-world engineering.

The RNG k–ε turbulence model adopted in this study has high accuracy in eddy current simulation. It can more accurately depict the solar chimney's turbulent flow and heat transmission properties. Mutual verification the result of numerical simulation and theoretical analysis to make the research more comprehensive and reliable. This investigation expands the theoretical research idea for the analysis of turbulent convection heat transfer characteristics in an open cavity. It has a certain theoretical significance for solar chimney engineering design.

2 | SCALING ANALYSIS

Figure 1A depicts the physical representation of the combined solar chimney natural ventilation system, which consists of a vertical air channel and a slanted air channel. The left side wall is a glass plate (separated from the outside world), and the right side wall is an absorbing wall. The width of the chimney W is horizontal distance among the absorbing wall and the glass plate, l is the length of the chimney in the sloping section, H is the height of the vertical section, and h is the height of the bottom entrance of the chimney. Among them, the inclination angle of the chimney inclined section $\alpha = 45°$,

20500505, 2024, 5, Downloaded from https://scijournals.onlinelibrary.wiley.com/doi/10.1002/ese3.1729 by Cochrane France, Wiley Online Library on [05/06/2025]. See the Terms and Conditions (https://onlinelibrary.wiley.com/terms-and-conditions) on Wiley Online Library for rules of use; OA articles are governed by the applicable Creative Commons License

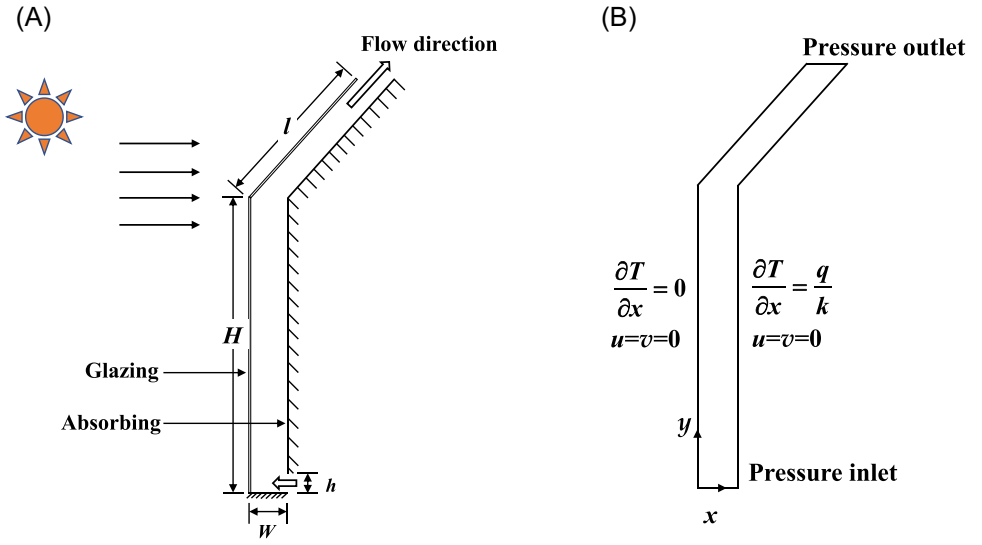


FIGURE 1 Combined solar chimney model. (A) Schematic diagram. (B) Boundary conditions.

and other dimensions of the chimney are explained in Table 3. The sun serves as a heat source, absorbing solar energy through its vertical and inclined endothermic walls, which then heat the air inside the chimney. The air inside and outside the chimney produces a temperature difference, which causes a density difference, forming a hot pressure to provide buoyancy for air flow. The effect of thermal buoyancy, the channel's flow rises and exits at its top outlet into the surrounding environment.

Figure 1B shows the 2D boundary conditions of the solar chimney model. The glass plate is the radiation boundary ($\partial T/\partial x = 0$), the absorbing wall is the fixed heat flux boundary ($q \sim k\partial T/\partial x$), the bottom inlet is the pressure inlet, and the top outlet is the pressure outlet ($\partial T/\partial y = 0$), inlet and outlet turbulence intensity $I = 2\%$. Ambient temperature $T_0 = 298.15$ K. Nouanégué et al. demonstrated that the influence of wall thickness on ventilation effect was negligible compared with Ra and chimney geometry parameters.[34] The effect of wall thickness is not taken into account in this paper. Furthermore, the following assumptions are made: the external environment is steady, wall heat storage is neglected, and the gas in the model is an incompressible Newtonian fluid.

The continuity equation, Navier–Stokes equations based on the Boussinesq approximation, and the energy equation all control the flow through the solar chimney channel.

The continuity equation is:

$$\frac{\partial \mathrm{u}}{\partial x} + \frac{\partial \mathrm{v}}{\partial \mathrm{y}} = 0. \tag{1}$$

The momentum equation is:

$$\frac{\partial u}{\partial t} + u\frac{\partial u}{\partial x} + v\frac{\partial u}{\partial y} = -\frac{1}{\rho}\frac{\partial p}{\partial x} + \nu'\left(\frac{\partial^2 u}{\partial x^2} + \frac{\partial^2 u}{\partial y^2}\right), \tag{2}$$

$$\frac{\partial v}{\partial t} + u\frac{\partial v}{\partial x} + v\frac{\partial v}{\partial y} = -\frac{1}{\rho}\frac{\partial p}{\partial y} + \nu'\left(\frac{\partial^2 v}{\partial x^2} + \frac{\partial^2 v}{\partial y^2}\right) + g\beta(T - T_0), \tag{3}$$

where u and v are the the velocity in x and y directions, p is pressure, ρ is the air density, $\nu' = \nu_t + \nu$, ν' is the sum of turbulent and laminar viscosity coefficients, ν_t, ν is the turbulence and laminar viscosity coefficient, g is the acceleration of gravity in the y direction, β is the coefficient of air expansion, T_0 is the initial temperature.

The energy equation is:

$$\frac{\partial T}{\partial t} + u\frac{\partial T}{\partial x} + \mathrm{v}\frac{\partial T}{\partial \mathrm{y}} = \Gamma\left(\frac{\partial^2 T}{\partial x^2} + \frac{\partial^2 T}{\partial \mathrm{y}^2}\right) + S_T, \tag{4}$$

$$\Gamma = \frac{\lambda}{c_p} + \frac{\nu_t}{\sigma_t} = \frac{\nu}{\mathrm{Pr}} + \frac{\nu_t}{\sigma_t}, \tag{5}$$

where Γ is the generalized diffusion coefficient, ν/Pr is the caused by molecular diffusion, ν_t/σ_t is the caused by turbulent fluctuations, S_T is the viscous dissipation term.

The k-equation is:

$$\frac{\partial}{\partial t}(\rho k) + \frac{\partial}{\partial x_i}(\rho k u_i) = \frac{\partial}{\partial x_j}\left(\sigma_k \mu_{eff}\frac{\partial k}{\partial x_j}\right) + G_k + G_b - \rho\varepsilon - Y_m + S_k, \tag{6}$$

20500505, 2024, 5, Downloaded from https://scijournals.onlinelibrary.wiley.com/doi/10.1002/esc3.1729 by Cochrane France, Wiley Online Library on [05/06/2025]. See the Terms and Conditions (https://onlinelibrary.wiley.com/terms-and-conditions) on Wiley Online Library for rules of use; OA articles are governed by the applicable Creative Commons License

The ε-equation is:

$$\frac{\partial}{\partial t}(\rho\varepsilon) + \frac{\partial}{\partial x_i}(\rho\varepsilon u_i) = \frac{\partial}{\partial x_j}\left(\sigma_\varepsilon \mu_{eff}\frac{\partial \varepsilon}{\partial x_j}\right) + C_{1\varepsilon}\frac{\varepsilon}{k}(G_k + C_{3\varepsilon}G_b) - C_{2\varepsilon}\rho\frac{\varepsilon^2}{k} - R + S_\varepsilon, \quad (7)$$

where G_k is the term for the creation of turbulent kinetic energy caused by an average velocity gradient, G_b is the buoyancy-based turbulent kinetic energy generation, Y_m is the contribution of pulsation dissipation to dissipation rate in compressible turbulent flow, σ_k and σ_ε are the k and ε turbulent Prandtl number respectively, S_k and S_ε are source term.

$$\mu_{eff} = C'_\mu \rho k^2/\varepsilon, \quad (8)$$

$$R = \frac{\rho C'_\mu \eta^3(1-\eta/\eta_0)}{1+\beta\eta^3}\frac{\varepsilon^3}{k}, \quad (9)$$

where η is the time scale proportion of turbulence to the average tension.[35] The constants in the RNG k–ε model are: $C'_\mu = 0.0845$, $C_{1\varepsilon} = 1.42$, $C_{2\varepsilon} = 1.68$, $\sigma_k = 1.393$, $\eta_0 = 4.38$.

Fluid heat transfer depends on three dimensionless control parameters, namely Rayleigh number (Ra), Prandtl number (Pr), the aspect ratio of chimney (A), and length ratio of inclined section to vertical section (l/H). Ra, Pr, and A are defined as follows:

$$Ra = \frac{g\beta q H^4}{k\nu\kappa}, \quad (10)$$

$$\mathrm{Pr} = \frac{\nu}{\kappa}, \quad (11)$$

$$A = \frac{H}{W}. \quad (12)$$

Then, scaling analysis is performed using Equations (1)–(4). Two possible cases with and without obvious thermal boundary layers are considered, respectively. Scaling analysis is applied to calculate the scales of thermal boundary layer thickness, time to reach full development, temperature, speed, and steady-state rate of mass flow.

2.1 | Flow regime with an obvious thermal boundary layer

The solar chimney's absorbing wall is equivalent to the heat source with constant q heat flow. In the initial stage, the difference of temperature will cause the transfer of heat from the absorbing wall to the ambient fluid, thus forming a thermal boundary layer of thickness δ_T near the absorbing wall. Heat flux between the ambient fluid and the heat absorption wall is $q \sim k\Delta T/\delta_T$. δ_T is the thermal boundary layer thickness, k is the thermal conductivity of fluid, and ΔT is temperature difference between the environment fluid and the heat absorption wall[9]:

$$\Delta T \sim \frac{q\delta_T}{k}. \quad (13)$$

The unsteady term in Equation (4) is $O[\Delta T/t]$, $O[\nu\Delta T/H]$ is the convection term, and the thermal conductivity term is $O[\Gamma\Delta T/\delta T^2]$. The unsteady term and the convection term in Equation (4) are compared as follows:

$$\frac{\Delta T/t}{\mathrm{v}\Delta T/H} \sim \frac{H}{\mathrm{v}t}. \quad (14)$$

Since the time is short enough, $H/vt \gg 1$, the equilibrium at this time is among the unsteady and the thermal conductivity terms, and then the thickness δ_T of the thermal boundary layer is as follows[4]:

$$\delta_T \sim (\Gamma t)^{1/2}. \quad (15)$$

Scale in Equation (15) remains until the convective term plays a dominant role (or reaches the quasi-steady stage).

In Equation (3), where the unsteady term is $O[v/t]$, the convection term is $O[v^2/H]$, the viscous term is $O[v'v/{\delta_T}^2]$, and the buoyancy term is $O[g\beta\Delta T]$, then the ratio between the unsteady term and the convection term is:

$$\frac{\mathrm{v}/t}{\mathrm{v}^2/H} \sim \frac{H}{\mathrm{v}t}. \quad (16)$$

The proportion of the unsteady to the viscous terms is:

$$\frac{\mathrm{v}/t}{\nu'\mathrm{v}/\delta_T^2} \sim \frac{\delta_T^2}{\nu' t} \sim \frac{\Gamma}{\nu'} \sim \frac{1}{\left(1+\frac{\nu_t}{\nu}\right)\sigma_t} + \frac{1}{\left(1+\frac{\nu}{\nu_t}\right)\mathrm{Pr}}. \quad (17)$$

Scale (16) shows that the unstable term is significantly bigger than the convective term in the case of a very short time. Scale (17) shows that the proportion of the unstable and viscous term is related to the turbulent Prandtl number σ_t and Pr. For $\sigma_t \gg 1$, $\mathrm{Pr} \gg 1$, the equilibrium is among the viscous term and the buoyant term. When $\mathrm{Pr} \ll 1$, the equilibrium is among the unstable and the buoyancy terms.[12] For $\mathrm{Pr} = 0.71$, the

20500505, 2024, 5, Downloaded from https://scijournals.onlinelibrary.wiley.com/doi/10.1002/ese3.1729 by Cochrane France, Wiley Online Library on [05/06/2025]. See the Terms and Conditions (https://onlinelibrary.wiley.com/terms-and-conditions) on Wiley Online Library for rules of use; OA articles are governed by the applicable Creative Commons License

speed scale v_T at the vertical in the thermal boundary layer is obtained by balancing the unstable and buoyant terms in the vertical momentum equation:

$$v_T \sim \frac{Ra\mathrm{Pr}\kappa^2\Gamma^{1/2}}{H^4}t^{3/2}. \tag{18}$$

According to Bejan,[36] the product of Ra and Pr is called Boussinesq number, namely $Bo = Ra\mathrm{Pr}$.

Then the above scale is:

$$v_T \sim \frac{Bo\kappa^2\Gamma^{1/2}}{H^4}t^{3/2}. \tag{19}$$

With the evolution of time, the flow enters the convective stage. Based on the equilibrium among the convective and thermal conductivity terms in Equation (4), The period of time needed for the boundary layer to develop and achieve the quasi-steady state can be obtained:

$$t_s \sim \frac{H^2}{Bo^{2/5}\kappa^{4/5}\Gamma^{1/5}}. \tag{20}$$

The thermal boundary layer thickness $\delta_{T,s}$ at time t_s is:

$$\delta_{T,s} \sim \frac{H\Gamma^{2/5}}{Bo^{1/5}\kappa^{2/5}}. \tag{21}$$

Then, the temperature improvement scale ΔT in the boundary layer during the quasi-steady state is:

$$\Delta T \sim \frac{qH\Gamma^{2/5}}{kBo^{1/5}\kappa^{2/5}}. \tag{22}$$

In the quasi-steady state, the vertical speed scale $v_{T,s}$ of the boundary layer is:

$$v_{T,s} \sim \frac{Bo^{2/5}\kappa^{4/5}\Gamma^{1/5}}{H}. \tag{23}$$

After reaches quasi-steady state, mass flow rate m is:

$$m \sim \rho \mathrm{v}_{T,s}\delta_{T,s} \sim \rho Bo^{1/5}\kappa^{2/5}\Gamma^{3/5}. \tag{24}$$

Inside layer and outside layer are the two divisions of the velocity boundary layer. The inner velocity boundary layer is controlled by inertial-viscous equilibrium in the close-wall region, represented by the subscript i, while the outside speed boundary layer is controlled by the buoyancy-viscous equilibrium. In the inside velocity boundary layer, the balance among the unstable and the viscous terms in Equation (3) determines the inner speed boundary layer thickness δ_{vi}[37]:

$$\delta_{\mathrm{vi}} \sim (\nu' t)^{1/2}. \tag{25}$$

According to scales (21) and (22), the thickness $\delta_{vi,s}$ of the inside boundary layer in the quasi-steady stage can be obtained:

$$\delta_{\mathrm{vi},s} \sim \left(\frac{\nu'}{\Gamma}\right)^{1/2}\delta_{T,s}. \tag{26}$$

When the boundary layer develops to the quasi-steady stage, for $\mathrm{Pr} = 0.71$, the outer velocity boundary layer and the thermal boundary layer have the same thickness,[36] as shown in Figure 2B. Therefore, the thickness of the outside speed boundary layer thickness scale δ_{vo} equal to the thermal boundary layer thickness scales $\delta_{T,S}$ namely

$$\delta_{\mathrm{vo},s} \approx \delta_{T,s}. \tag{27}$$

Consistent with the conclusions drawn by He[12] and Rakesh Khanal,[13] the above scaling correlations is only applicable for $\delta_{T,s} < W$. Only if the thickness of the thermal boundary layer at any place in the vertical direction of the chimney meets $\delta_{T,s} < W$, then can the development of thermal boundary layer be free from restriction and interference as in large space. If $\delta_{T,s} > W$, the thermal boundary layer cannot free development, which is the characteristic of natural convective heat transfer in finite space. Therefore, the requirement for the presence of an obvious thermal boundary layer can be obtained from $\delta_{T,s} < W$, as shown in scale (28)

$$Ra > \frac{A^5\Gamma^2}{\mathrm{Pr}\kappa^2}. \tag{28}$$

According to $\delta_{T,s} > W$, the interval without obvious thermal boundary layer flow regime can be obtained as follows:

$$Ra < \frac{A^5\Gamma^2}{\mathrm{Pr}\kappa^2}. \tag{29}$$

According to the above scaling analysis and the study of Rakesh Khanal,[13] there are two possibilities:

1. As $Ra > A^5\Gamma^2/\mathrm{Pr}\kappa^2$, the of the thermal boundary layer's thickness in the stable stage is smaller than the width of the chimney, and an obvious thermal boundary layer flow pattern dominated by convection is formed in the quasi-steady stage.

20500505, 2024, 5, Downloaded from https://scijournals.onlinelibrary.wiley.com/doi/10.1002/esc3.1729 by Cochrane France, Wiley Online Library on [05/06/2025]. See the Terms and Conditions (https://onlinelibrary.wiley.com/terms-and-conditions) on Wiley Online Library for rules of use; OA articles are governed by the applicable Creative Commons License

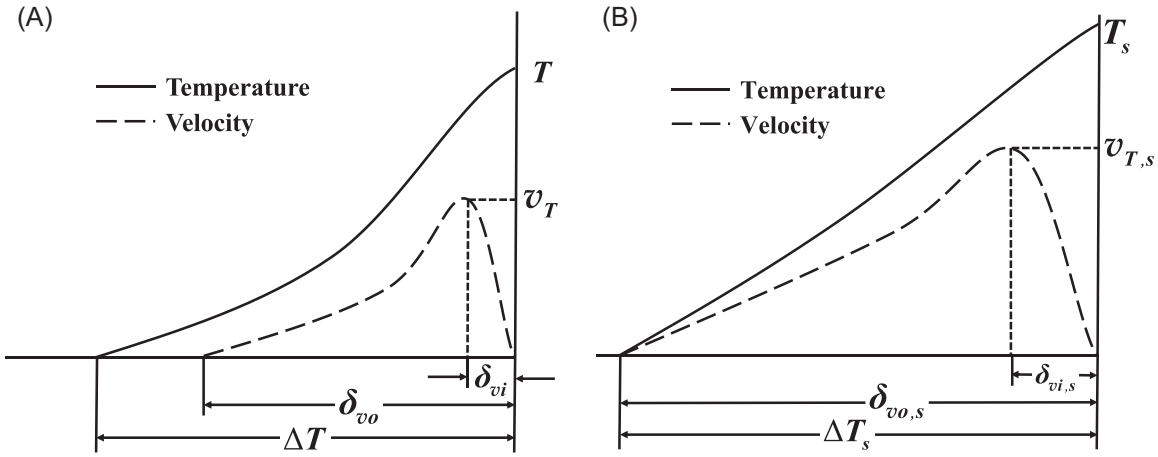


FIGURE 2 Schematic diagram of the initial and quasi-steady stages of boundary layer development. (A) In the initial stage. (B) In the quasi-steady stage.

2. When $Ra < A^5\Gamma^2/\mathrm{Pr}\kappa^2$, the thermal boundary layer thickness extends over the whole breadth of the chimney before the flow reaches the convection heat conduction equilibrium. A flow state without obvious thermal boundary layer dominated by thermal conductivity is formed. These important scale relationships of this flow pattern will be discussed in Section 2.2.

2.2 | Flow regime without an obvious thermal boundary layer

When Ra is less than the critical value, the thermal boundary layer will finally grow to the entire breadth of the chimney until thermal conductivity and convection are balanced. This situation often occurs when the width of a solar chimney is small or the heat absorbed by the absorbing wall is small. In this state of flow, the thermal boundary layer thickness scale reaches $\delta_T \sim W$ at $t \sim t_w$[13]:

$$(\Gamma t_w)^{1/2} \sim W. \tag{30}$$

When the thermal boundary layer thickness δ_T reaches the chimney width W, the time scale t_w is obtained:

$$t_w \sim \frac{W^2}{\Gamma}. \tag{31}$$

Scale (28) may additionally be obtained by contrasting different time scales. When the time scale t_s in scale (20) is smaller than the time scale t_w, a distinct thermal boundary layer will appear.[13]

From scales (13) and (19), the corresponding temperature growth scale ΔT_w in the chimney and vertical velocity scale $v_{T,w}$ of the boundary layer can be obtained:

$$\Delta T_w \sim \frac{qW}{k}, \tag{32}$$

$$\mathrm{v}_{T,w} \sim \frac{Bo\kappa^2}{\Gamma W A^4}. \tag{33}$$

So the viscous term in the vertical momentum Equation (3) is $O[v'v/W^2]$. When $t \sim t_w$, the proportion between the unsteady and the convective terms show that the former is more significant than the latter as $H > vt$. According to the proportion of unsteady to viscous terms, the unstable term is more significant than the viscous term as $\mathrm{Pr} = 0.71$. Therefore, the equilibrium at $t \sim t_w$ is controlled by unsteady-buoyancy mechanism.

The thermal boundary layer thickness for $t > t_w$ is equal to the chimney's breadth. At this point, heat conduction is still dominant, and convection is not enough to exit the heat released by the absorbing wall to the thermal boundary layer. Therefore, the temperature of the whole chimney passage increases with the increase of time. Through energy balance and $\kappa = k/\rho c_p$, it can be obtained that the temperature increase $\Delta T_w{}^+$ in the chimney is

$$qH \sim \rho \mathrm{c_p} HW \frac{\Delta T_{w^+}}{t}, \tag{34}$$

$$\Delta T_{w^+} \sim \frac{q\kappa}{kW} t. \tag{35}$$

The above correlation shows that when the thermal boundary layer covers the entire breadth of the chimney,

20500505, 2024, 5, Downloaded from https://scijournals.onlinelibrary.wiley.com/doi/10.1002/ese3.1729 by Cochrane France, Wiley Online Library on [05/06/2025]. See the Terms and Conditions (https://onlinelibrary.wiley.com/terms-and-conditions) on Wiley Online Library for rules of use; OA articles are governed by the applicable Creative Commons License

the temperature rises linearly with passing time. Due to the rise in buoyancy, the airflow in the chimney accelerates as the temperature in the chimney rises. According to the ratio of the unsteady term to the viscous term in the vertical momentum Equation (3), when $t > (\Gamma/\nu')t_w$, the viscous term is more significant than the unstable term. Consequently, for $t_w < t < (\Gamma/\nu')t_w$, the flow is controlled by the unsteady-buoyancy mechanism, namely

$$\frac{\mathrm{v}}{t} \sim g\beta\Delta T_{w^+}. \tag{36}$$

The boundary layer vertical velocity scale v_T under unsteady-buoyancy equilibrium is obtained:

$$\mathrm{v}_T \sim \frac{\kappa^3 Bo}{H^4 W} t^2. \tag{37}$$

The velocity scale (37) describes thermal conductivity, where the velocity increases with t^2 increasing. This velocity scale is applied until $t = t_f$, when there is a balance among the heat absorbed by the endothermic wall and the heat taken away by convection in the chimney. As a result, the stable state time scale t_f can be obtained through the balance of energy:

$$qH \sim \rho \mathrm{c_p} \mathrm{v}_{T,f} W \Delta T_{w^+}, \tag{38}$$

$$t_f \sim \frac{H^{5/3} W^{1/3}}{\kappa Bo^{1/3}}. \tag{39}$$

The time scale shown above is accurate for $t_f < (\Gamma/\nu')t_w$, that is, for $Ra < A^5\Gamma^2/\mathrm{Pr}\kappa^2 < A^5\nu'^3\mathrm{Pr}\kappa^3$. When the diffusion time t_f is reached, the flow is controlled by unsteady-buoyancy mechanism. The scales corresponding to temperature difference $\Delta T_w{}^+{}_{,f}$, velocity $v_{T,f}$ and mass flow rate m are:

$$\Delta T_{w^+,f} \sim \frac{qWA^2}{kBo^{1/3}}, \tag{40}$$

$$\mathrm{v}_{T,f} \sim \frac{\kappa Bo^{1/3}}{H^{2/3} W^{1/3}}, \tag{41}$$

$$m \sim \rho \mathrm{v}_{T,f} W \sim \rho \frac{\kappa Bo^{1/3}}{A^{2/3}}. \tag{42}$$

2.3 | Summary of the scaling analysis

Figure 3 depicts several flow patterns for the development of the flow in the solar chimney. Depending on *Ra*, there may be two primary flow regimes in the solar chimney. Air flow is regulated by convection when the thermal boundary layer thickness, $\delta_{T,s} < W$, is less than the chimney's breadth in a quasi-steady state. Conduction, which lacks an obvious thermal boundary layer, dominates this flow when the thickness of the thermal boundary layer is equal to the width of the chimney channel ($\delta_T \sim W$).

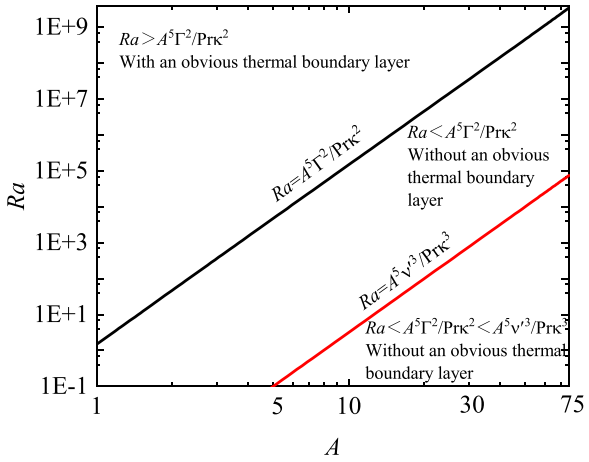


FIGURE 3 Schematic diagram of possible flow patterns.

The detailed transient characteristics, control mechanisms, and crucial dimensional correlations of fluid development are shown in Table 1. Use "" to represent the corresponding dimensionless scale relationship. For example, (19) represents the dimensionless scale relation, and (19') represents the corresponding dimensionless scale relation. The dimensionless scales in Table 1 use the following scales: the velocity scale $\kappa^2/H\Gamma$, the temperature scale qH/k, the time scale H^2/Γ, and the mass outflow rate scale $\rho\kappa$. In Table 1, V_T is the dimensionless velocity scale, τ is the dimensionless time, θ is the dimensionless temperature, and M is the dimensionless mass flow rate. For the transient flow that forms a boundary layer on the absorb wall with constant heat flux applied, it mainly passes through the initial stage, the transition stage and the full development stage (this is also verified in the analysis of *Nu* in Section 3). The wall temperature, thermal boundary layer's thickness, velocity boundary layer's thickness, vertical speed in the boundary layer, and the amount of time needed for the boundary layer to form and reach a quasi-steady state are the main parameters to express the instantaneous flow characteristics. The parameters representing the instantaneous flow properties and the qualitative relationship between these parameters and the control parameters are obtained in the scaling analysis at each stage. The plausibility of these obtained qualitative relations will be mutually verified with numerical simulation results in Section 3.

20500505, 2024, 5, Downloaded from https://scijournals.onlinelibrary.wiley.com/doi/10.1002/esc3.1729 by Cochrane France, Wiley Online Library on [05/06/2025]. See the Terms and Conditions (https://onlinelibrary.wiley.com/terms-and-conditions) on Wiley Online Library for rules of use; OA articles are governed by the applicable Creative Commons License

TABLE 1 Flow development and important scale correlations under different control mechanisms.

Regime	Time	Control mechanisms	Important scale correlations			
			Dimensional scale correlations		Dimensionless scale correlations	
With an obvious thermal boundary layer $Ra > \frac{A^5\Gamma^2}{Pr\kappa^2}$	$t < t_s < t_w$	Unsteady-buoyancy equilibrium dominated by thermal conductivity	$v_T \sim \frac{Bo\kappa^2\Gamma^{1/2}}{H^4}t^{3/2}$	(19)	$V_T \sim Bo\tau^{3/2}$	(19′)
	$t \geq t_s$	Thermal conduction-convection equilibrium with an obvious thermal boundary layer	$t_s \sim \frac{H^2}{Bo^{2/5}\kappa^{4/5}\Gamma^{1/5}}$	(20)	$\tau_s \sim \left(\frac{\Gamma}{\kappa}\right)^{4/5}Bo^{-2/5}$	(20′)
			$\Delta T \sim \frac{qH\Gamma^{2/5}}{kBo^{1/5}\kappa^{2/5}}$	(22)	$\theta \sim \left(\frac{\Gamma}{\kappa}\right)^{2/5}Bo^{-1/5}$	(22′)
			$m \sim \rho v_{T,s}\delta_{T,s} \sim \rho Bo^{1/5}\kappa^{2/5}\Gamma^{3/5}$	(24)	$M \sim \left(\frac{\Gamma}{\kappa}\right)^{3/5}Bo^{1/5}$	(24′)
Without an obvious thermal boundary layer $Ra < \frac{A^5\Gamma^2}{Pr\kappa^2}$	$t \sim t_w$	Unsteady-buoyancy equilibrium dominated by thermal conductivity	$v_T \sim \frac{Bo\kappa^2\Gamma^{1/2}}{H^4}t^{3/2}$	(19)	$V_T \sim Bo\tau^{3/2}$	(19′)
			$t_w \sim \frac{W^2}{\Gamma}$	(31)	$\tau_w \sim A^{-2}$	(31′)
	$t_w < t < t_f$		$\Delta T_{w^+} \sim \frac{q\kappa}{kW}t$	(36)	$\theta_{w^+} \sim \frac{\kappa}{\Gamma}A\tau$	(36′)
	$t \geq t_f$	Thermal conduction-convection equilibrium without an obvious thermal boundary layer	$m \sim \rho v_{T,f}W \sim \rho\frac{\kappa Bo^{1/3}}{A^{2/3}}$	(42)	$M \sim \left(\frac{Bo}{A^2}\right)^{1/3}$	(42′)

3 | VERIFICATION OF NUMERICAL SIMULATION AND SCALING ANALYSIS

In this section, ANSYS Fluent is used for numerical simulation to verify the important scale relationships in Table 1. The 2D model is selected on the basis that 2D simulation can capture the physical characteristics of air flow in the chimney passage, and the difference in results is negligible. This conclusion has been confirmed by the studies of Gong et al.,[38] Pasut et al.,[39] and Zamora et al.[40] The dimensionless form corresponding to Equations (1)–(4) is as follows:

$$\frac{\partial U}{\partial X} + \frac{\partial V}{\partial Y} = 0, \tag{43}$$

$$\frac{\partial U}{\partial \tau} + \frac{\kappa^2}{\Gamma^2}\left(U\frac{\partial U}{\partial X} + V\frac{\partial U}{\partial Y}\right) = -\frac{\kappa^2}{\Gamma^2}\frac{\partial P}{\partial X} + \frac{\nu'}{\Gamma}\left(\frac{\partial^2 U}{\partial X^2} + \frac{\partial^2 U}{\partial Y^2}\right), \tag{44}$$

$$\frac{\partial V}{\partial \tau} + \frac{\kappa^2}{\Gamma^2}\left(U\frac{\partial V}{\partial X} + V\frac{\partial V}{\partial Y}\right) = -\frac{\kappa^2}{\Gamma^2}\frac{\partial P}{\partial Y} + \frac{\nu'}{\Gamma}\left(\frac{\partial^2 V}{\partial X^2} + \frac{\partial^2 V}{\partial Y^2}\right) + Bo\theta, \tag{45}$$

$$\frac{\partial \theta}{\partial \tau} + \frac{\kappa^2}{\Gamma^2}\left(U\frac{\partial \theta}{\partial X} + V\frac{\partial \theta}{\partial Y}\right) = \frac{\partial^2 \theta}{\partial X^2} + \frac{\partial^2 \theta}{\partial Y^2}, \tag{46}$$

$$\frac{\partial}{\partial \tau}\left(\frac{\rho k\Gamma}{H^2}\right) + \frac{\partial}{\partial X_i}\left(\frac{\rho k\kappa^2 U_i}{\Gamma H^2}\right) = \frac{\partial}{\partial X_j}\left(\frac{\sigma_k \mu_{eff}}{H^2}\frac{\partial k}{\partial X_j}\right) + G_k + G_b - \rho\varepsilon - Y_m + S_k, \tag{47}$$

$$\frac{\partial}{\partial \tau}\left(\frac{\rho\varepsilon\Gamma}{H^2}\right) + \frac{\partial}{\partial X_i}\left(\frac{\rho\varepsilon\kappa^2 U_i}{\Gamma H^2}\right) = \frac{\partial}{\partial X_j}\left(\frac{\sigma_\varepsilon \mu_{eff}}{H^2}\frac{\partial \varepsilon}{\partial X_j}\right) + C_{1\varepsilon}\frac{\varepsilon}{k}(G_k + C_{3\varepsilon}G_b) - C_{2\varepsilon}\rho\frac{\varepsilon^2}{k} - R + S_\varepsilon, \tag{48}$$

where $X = x/H$, $Y = y/H$, $\tau = t/(H^2/\Gamma)$, $\theta = (T - T_0)/(qH/k)$, $U = u/(\kappa^2/H\Gamma)$, $V = v/(\kappa^2/H\Gamma)$, $P = p/(\kappa^2/H\Gamma)^2$.

Where X, Y are dimensionless coordinates; U, V are dimensionless velocity in the X and Y directions; P is dimensionless pressure; θ is dimensionless temperature; τ is dimensionless time.

The RNG k–ε model is able to analyze turbulent vortices more accurately and produce more accurate calculation results because of the vortex areas that are present inside the chimney.[41] Therefore, the RNG k–ε model is chosen in the simulation. A radiation model needs to be added to the calculation model because there

20500505, 2024, 5, Downloaded from https://scijournals.onlinelibrary.wiley.com/doi/10.1002/ese3.1729 by Cochrane France, Wiley Online Library on [05/06/2025]. See the Terms and Conditions (https://onlinelibrary.wiley.com/terms-and-conditions) on Wiley Online Library for rules of use; OA articles are governed by the applicable Creative Commons License

TABLE 2 Validity verification of turbulence model.

Solar radiation intensity (W/m^2)	The ventilation of the test[23] M_e	The ventilation of numerical simulation M_c	Deviation $(M_e-M_c)/M_e$ (%)
200	0.989	0.904	8.57
400	1.501	1.365	9.06
600	1.794	1.590	11.37
800	1.901	1.767	7.05
1,000	2.161	1.914	11.39

is also considerable radiation heat transfer on the inner surface of the glass plate in the heat-collecting face of the heat-absorbing plate.[42] The DO model is selected in this case. In the simulation, enhanced wall treatment is used.

In this study, the initial flow field is set to be isothermal static, that is, $T = T_0$. The boundary conditions for the numerical simulation are displayed in Figure 1B and are as follows: the inlet is the pressure inlet ($P = 0$), the outlet is the pressure outlet ($P = 0$, $\partial\theta/\partial Y = 0$, $\partial U/\partial Y = 0$, $\partial V/\partial Y = 0$, $\theta = 0$), the heat absorbing wall is a fixed heat flow boundary ($U = V = 0$, $\partial\theta/\partial X = 1$), and the other walls are non-slip walls ($U = V = 0$, $\partial\theta/\partial X = 0$).

The finite volume method is used to discrete the governing equations. The diffusion term is discretized by the second-order central difference scheme, the convection term by the second-order upwind scheme, and the transient term by the second-order implicit time advance scheme. The SIMPLE algorithm is used to calculate the coupling between pressure and velocity. In addition to the energy equation, the convergence iteration residual of all equations is 10^{-6}, and the energy equation is 10^{-8}.

For this study, the following assumptions and simplifications are made to simplify the computation process: (1) The outdoor environment (solar radiation intensity and outdoor air temperature) does not change with time; (2) The flow in the chimney passage is turbulent; (3) Assume that the gas in the chimney passage is an incompressible Newtonian fluid; (4) The thickness of each wall of the chimney is ignored; (5) The calculation is simplified by Boussinesq hypothesis, and the density in the buoyancy term of the vertical momentum equation is considered as a function of temperature, while the density in other terms is a constant.

The numerical simulation and experimental study are contrasted to confirm the applicability of the turbulence model and boundary conditions. A physical model of a vertical solar chimney in 3D is built, with channel dimensions of 1025 mm in height, 925 mm in length, and 20 mm in width. Simulation results under different solar radiation intensities are compared with experiment data,[23] as shown in Table 2. The ventilation volume increases with the increase in solar radiation intensity. The overall trend of the numerical simulation results is consistent with the experimental results, and the deviation is less than 12%. Within the allowable range of error, the validity of the turbulence model and calculation method used in this paper are fully demonstrated.

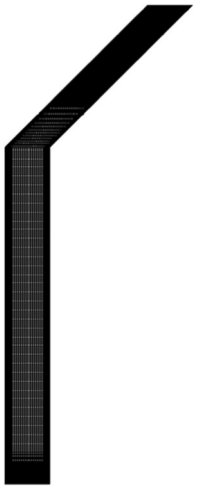


FIGURE 4 Grid diagram in the model calculation domain.

The reason for the error between numerical simulation and experiment are: (1) The experiment cannot exclude the interference of external factors such as wind, temperature, and humidity, while numerical simulation only involves hot pressure ventilation and will not be affected by external factors; (2) In the numerical simulation, some simplifications were made to the physical model, without considering the thickness of the heat absorbing plate. In the experiment, the heat-absorbing plate had a certain thickness; (3) In CFD simulation, mathematical models are established based on assumptions and simplifications, which cannot fully accurately reflect the complexity of flow and heat transfer in experiments.

Figure 4 shows the grid diagram of the combined solar chimney. The grid is encrypted at the inlet, outlet, and wall surface. The grid system is divided into structured grids and four sets of grids and time steps are used to verify the independence of the grids and time steps, ensuring the accuracy of the numerical calculations. As indicated in Figure 5A,B, the time series of dimensionless outlet mass flow rate when $A = 60.0$ and $Ra = 2.42 \times 10^{13}$, and the dimensionless velocity distribution along the chimney width at upper end of the chimney inlet when $A = 7.5$ and $Ra = 9.47 \times 10^{10}$ is in steady state are, respectively, illustrated. As seen in

20500505, 2024, 5, Downloaded from https://scijournals.onlinelibrary.wiley.com/doi/10.1002/ese3.1729 by Cochrane France, Wiley Online Library on [05/06/2025]. See the Terms and Conditions (https://onlinelibrary.wiley.com/terms-and-conditions) on Wiley Online Library for rules of use; OA articles are governed by the applicable Creative Commons License

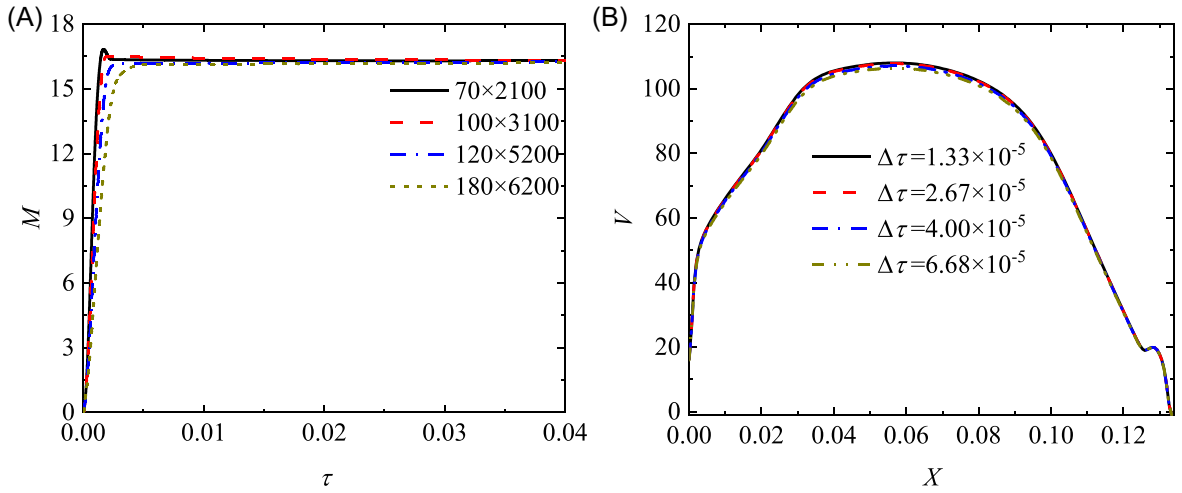


FIGURE 5 Grid and time step independence tests. (A) Time series of dimensionless outlet mass flow rate calculated by different grids at $A = 60$, $Ra = 2.42 \times 10^{13}$. (B) The dimensionless velocity distribution of the upper end of the chimney inlet along the width of the chimney at $A = 7.5$, $Ra = 9.47 \times 10^{10}$ in steady state.

Figure 5A, in the short time after flow start-up, with the increase in mesh number, the time to reach the full development stage is longer. This is due to the computational complexity and data transmission between grid nodes both increase with the increase in grid number, while the computational efficiency decreases. This increases the time required for computing to reach the full development stage. It is important to note that the minus velocity at $X = 0.133$ shown in Figure 5B is cause of the fact that the airflow is a vertical channel connected to the chimney by a horizontal inlet. The direction of airflow will shift by 90°, and its flow state will alter dramatically. Moreover, the negative velocity will accelerate the flow of air into the chimney, enhancing the ventilation capacity. As can be seen from Figure 5, the numerical results obtained with the four grid systems and time steps are not significantly different during the fully developed stage, and the error is less than 2% after quantitative calculations. To obtain accurate simulation results within limited computing resources, grid 120×5200 and time step $\tau = 4.0 \times 10^{-5}$ are selected for calculation. All different case models have been verified for grid and time-step independence.

As shown in Table 3, the cases involved in the calculation of this paper are mainly considered with air as the fluid medium ($\mathrm{Pr} = 0.71$). Variations in the Ra number and the ratio A of the vertical height of the solar chimney to the width of the chimney have been considered. Solar chimneys can be applied to residential buildings, dormitories, and public buildings, so this paper selects three different aspect ratios of $A = 7.5$, 60.0, and 75.0 for analysis.

The Nusselt number is an essential dimensionless number that reflects the convective heat transfer capacity during the sudden application of heating flux on the inner wall of a combined solar chimney cavity. Figure 5 shows the results of 2D numerical simulations of the mean Nu time series of the absorbing wall. The mean Nu is defined as follows:

$$Nu = \frac{1}{L}\int \frac{\partial T}{\partial \mathrm{n}} dL. \tag{49}$$

In Equation (49), for the chimney vertical section $L = H$ and for the chimney inclined section $L = l$.

With time, the mean Nu of the absorbing wall first rises and then falls noticeably, followed by an oscillating state and then a stable state, as seen in Figure 6. It can be broken down into three phases: the initial phase, the transition phase, and the quasi-steady phase. After the onset of the flow, an extremely thin vertical boundary layer forms on the endothermic wall and rapidly develops due to the large temperature difference among the endothermic wall and the air near the wall. In this developing phase of the boundary layer, heat transfer is dominated by the internal fluid due to strong viscous forces and weak convection. As time goes on, the boundary layer will keep increasing during the rise of the airflow, and the boundary layer will sufficiently develop until a stable state is reached.

3.1 | Thermal flow structures under different flow patterns

The flow development in the solar chimney is analyzed in Section 2, where there may be flow states with or without a distinct thermal boundary layer. These flow

20500505, 2024, 5, Downloaded from https://scijournals.onlinelibrary.wiley.com/doi/10.1002/ese3.1729 by Cochrane France, Wiley Online Library on [05/06/2025]. See the Terms and Conditions (https://onlinelibrary.wiley.com/terms-and-conditions) on Wiley Online Library for rules of use; OA articles are governed by the applicable Creative Commons License

TABLE 3 Parameter setting of numerical simulation cases.

Case	Symbol	Line type	H (m)	l/H	A	q (W/m^2)	$Ra\left(Ra > \frac{A^5\Gamma^2}{Pr\kappa^2}\right)$	$Ra\left(Ra < \frac{A^5\Gamma^2}{Pr\kappa^2} < \frac{A^5\nu'^2}{Pr\kappa^3}\right)$
C_{y1}	○	—	3.0	0.67	7.5	2.34×10^{1}	7.60×10^{12}	
C_{y2}	×	----				7.35×10^{1}	2.39×10^{13}	
C_{y3}	□	·····				1.13×10^{2}	3.67×10^{13}	
C_{y4}	▷	···				2.36×10^{2}	7.67×10^{13}	
C_{y5}	☆	——				3.64×10^{2}	1.18×10^{14}	
C_{n1}	▼	—	12.0	0.20	60.0	1.20×10^{-3}		3.64×10^{8}
C_{n2}	■	——				1.60×10^{-3}		4.85×10^{8}
C_{n3}	●	----				2.40×10^{-3}		7.27×10^{8}
C_{n4}	▲	·····				3.20×10^{-3}		9.70×10^{8}
C_{y6}	◇	—				2.34×10^{1}	1.95×10^{15}	
C_{y7}	Δ	···				2.36×10^{2}	1.97×10^{16}	
C_{n5}	▸	···	15.0		75.0	2.00×10^{-3}		1.48×10^{9}
C_{n6}	◆	—				2.80×10^{-3}		2.07×10^{9}
C_{n7}	◂	——				3.40×10^{-3}		2.54×10^{9}
C_{n8}	★	—				4.00×10^{-3}		2.96×10^{9}
C_{y8}	◁	----				2.34×10^{1}	4.75×10^{15}	
C_{y9}	▽	·····				2.36×10^{2}	4.80×10^{16}	

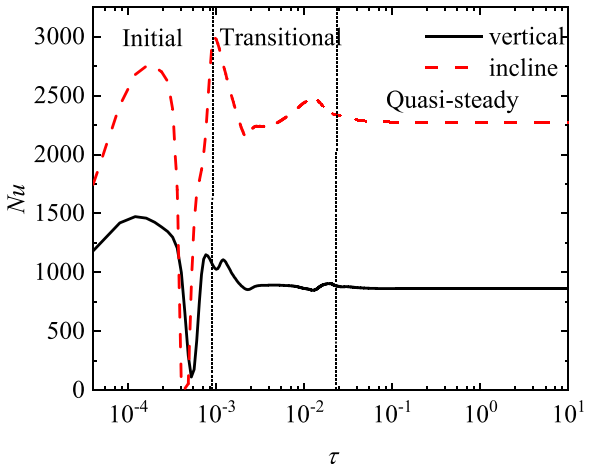


FIGURE 6 Time series of the average Nusselt number of the absorbing wall under C_{y3} ($A = 7.5$, $Ra = 1.34\times10^{11}$).

control mechanisms are illustrated in Figure 3. To further understand the flow structure under each flow state and explain the mechanism of flow and heat transfer characteristics in the chimney, the isotherms and streamlines in the chimney passage under the two flow states are shown in Figures 7 and 8.

To more intuitively understand the transient development process of natural air convection in the combined solar chimney, isotherms and streamlines at different times in the channel are given in Figure 7 when there is an obvious thermal boundary layer flow pattern (i.e., the typical case of high Ra flow state $Ra > A^5\Gamma^2/Pr\kappa^2$). The initial state of the flow field in the channel is isothermal static. A fixed heat flux boundary condition is imposed on the endothermic wall, leading to the formation of a thermal boundary layer near it. Due to heat conduction, the thickness of this thermal boundary layer gradually increases over time, its thickness is indicated by the scale (15), as depicted in Figure 7A. Under the dominant influence of thermal buoyancy, the fluid within the leading edge of the thermal boundary layer undergoes acceleration along the endothermic wall, giving rise to the formation of eddy currents within this layer. The presence of these vortices leads to convective dissipation of heat in the boundary layer. Figure 7B illustrates the morphology of the thermal boundary layer, with flow transitioning in this region. With the progressive advancement of the flow, a significant vortex with counter-rotating motion is generated at the outer periphery through the interaction of vortex clusters within the boundary layer, as depicted in Figure 7C. The boundary layer exhibits turbulent characteristics. The vortex acquires energy from the convective thermal boundary layer, leading to a gradual enlargement in its size, as depicted in Figure 7D. Once an equilibrium is reached between the thermal boundary layer and the

20500505, 2024, 5, Downloaded from https://scijournals.onlinelibrary.wiley.com/doi/10.1002/ese3.1729 by Cochrane France, Wiley Online Library on [05/06/2025]. See the Terms and Conditions (https://onlinelibrary.wiley.com/terms-and-conditions) on Wiley Online Library for rules of use; OA articles are governed by the applicable Creative Commons License

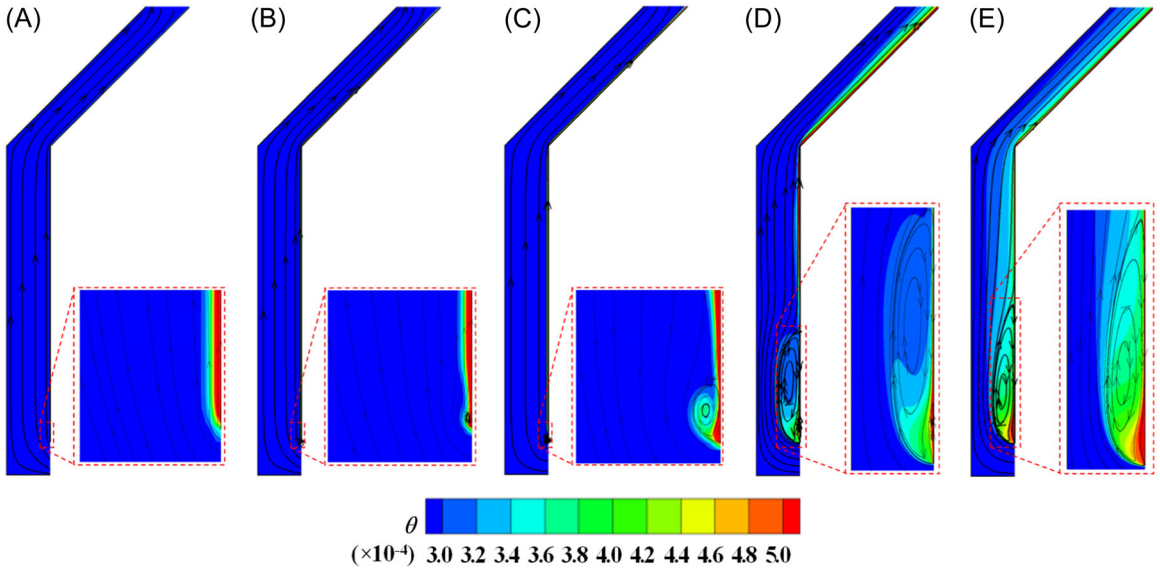


FIGURE 7 Evolution of temperature contours and streamlines in the combined solar chimney over time (case: C_{y3}). (A) $\tau = 1.60 \times 10^{-4}$, (B) $\tau = 4.81 \times 10^{-4}$, (C) $\tau = 8.82 \times 10^{-4}$, (D) $\tau = 5.73 \times 10^{-3}$, and (E) $\tau = 0.67$.

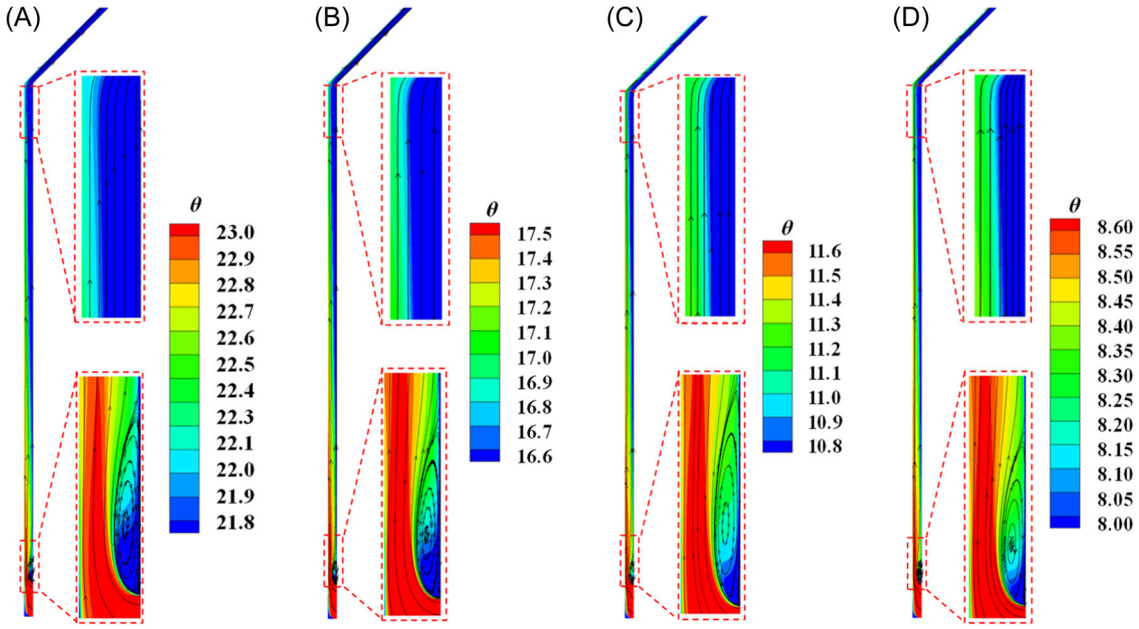


FIGURE 8 Isotherm and streamlines of combined solar chimney in full development stage under different *Ra*. (A) $Ra = 3.64 \times 10^8$, (B) $Ra = 4.85 \times 10^8$, (C) $Ra = 7.27 \times 10^8$, and (D) $Ra = 9.70 \times 10^8$.

channel flow, that is, after the time reaches scale (20), the flow reaches the full development stage. At this time, the thermal boundary layer thickness, temperature, wind speed and mass flow rate are represented by scales (21)–(24), respectively. The thermal boundary layer morphology and streamline distribution in the fully developed stage are shown in Figure 7E.

Without distinct thermal boundary layer flow pattern (i.e., the typical case of low *Ra* flow state $Ra < A^5\Gamma^2/\mathrm{Pr}\kappa^2$), the isotherm and streamlines diagram in the chimney passage at the full development stage are illustrated in Figure 8. For this flow state, the thermal boundary layer extends to the full chimney width before the flow reaches full development, which is represented by (31), where the equilibrium is controlled by the unsteady-buoyancy equilibrium. After that, the thermal boundary layer continues to develop under the unsteady-buoyancy control mechanism dominated by thermal conductivity, and the convection effect gradually increases, and is controlled by the heat conduction-convection equilibrium mechanism

20500505, 2024, 5, Downloaded from https://scijournals.onlinelibrary.wiley.com/doi/10.1002/ese3.1729 by Cochrane France, Wiley Online Library on [05/06/2025]. See the Terms and Conditions (https://onlinelibrary.wiley.com/terms-and-conditions) on Wiley Online Library for rules of use; OA articles are governed by the applicable Creative Commons License

when it reaches the full development stage. It can be clearly seen from the isotherm in Figure 8 that the thermal boundary layer covers the entire width of the chimney, so for the case of low *Ra*, there is without distinct thermal boundary layer inside the chimney. The streamlines are evenly distributed parallel to the wall, indicating that the flow is fully developed.

For $t > t_w$, the temperature in the chimney passage rises linearly with time as indicated by the scale (35′) until it approaches stable state. This scaling is verified by numerical simulation data shown in Figure 10. As shown in Figure 10, for $\tau/\tau_w > 1$, the temperature scale under different *Ra* increases linearly and gradually flattens out near the steady state.

3.2 | Verification of transient temperature and velocity scales

The dimensionless scaling correlations given in Table 1 are validated using numerical simulation findings in this and the following section, hence validating the dimensional analysis. Scale (19′) indicates a rise in thermal boundary layer velocity during the initial stages of development of the flow. The effective range of this scale can be up to t_s in the case of a thermal boundary layer that is well-defined and up to t_w in the absence of such a layer. Figure 9A illustrates the relation between V_T/Bo and $(\tau/\tau_s)^{3/2}$ when there is an obvious thermal boundary layer in stable state. As expected, there is a linear relationship between V_T/Bo and $(\tau/\tau_s)^{3/2}$ in the range of $\tau < \tau_s$, can be seen from the enlarged part $0 < (\tau/\tau_s) < 1.5$ in Figure 9A, which means that the formation of thermal boundary layer near the absorbing wall is controlled by heat conduction. Figure 9B shows the relationship between V_T/Bo and $(\tau/\tau_w)^{3/2}$ without distinct thermal boundary layer. The graphic demonstrates that the velocity data in various circumstances increases linearly with time when $\tau < \tau_w$, demonstrating the validity of the transient velocity scale.

3.3 | Verification of mass flow rate scale and temperature scale in a fully developed state

For the thermal boundary layer flow pattern of a solar chimney with an obvious thermal boundary layer, the mass rate of flow scale in steady-state is determined by (24′). As shown in Figure 11A, the numerical simulation results are contrasted to the scaling analysis results. It can be seen that the fit to the results of the numerical simulations lies approximately on a straight line. The mass flow rate of numerical calculation shows a linear relationship with scale prediction. Scale (24′) can therefore accurately represent the steady-state mass rate of flow of solar chimney with an obvious thermal boundary layer flow regime. For the flow regime without obvious thermal boundary layer, the mass flow rate scale in steady-state is determined by (42′). The results of the numerical simulation at different *Ra* are contrasted with the scaling analysis results. Figure 11B clearly shows the linear relationship among the results of numerical simulation and scale analysis. It is confirmed that the scale (42′) is correct in predicting the mass flow rate without a distinct thermal boundary layer flow state. Figure 12 verifies the validity of temperature scale (22′)

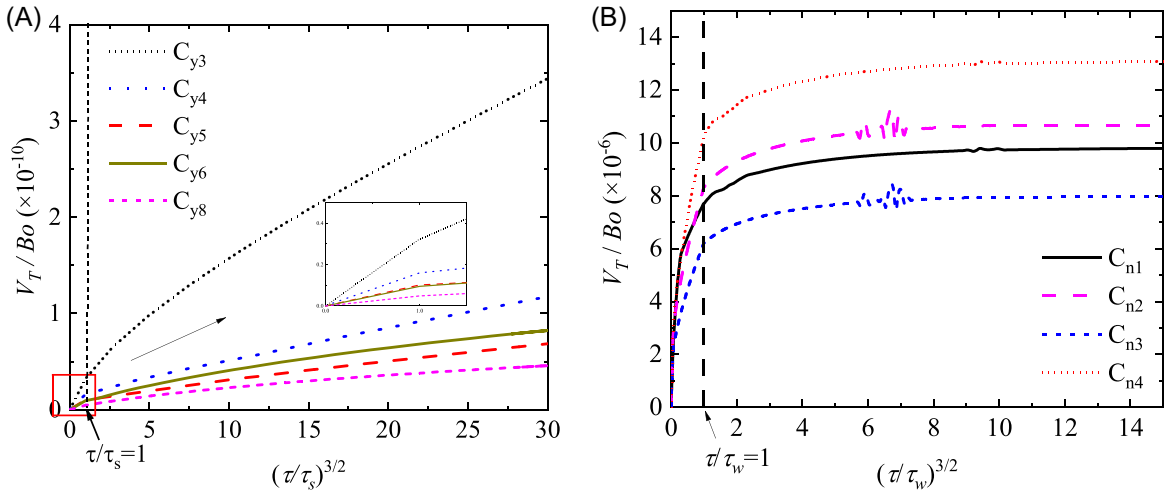


FIGURE 9 Verification of vertical velocity scale in the thermal boundary layer. (A) The velocity scales of the initial stage with distinct thermal boundary layer: V_T/Bo and $(\tau/\tau_s)^{3/2}$. (B) The velocity scales of the initial stage without distinct thermal boundary layer: V_T/Bo and $(\tau/\tau_w)^{3/2}$.

20500505, 2024, 5, Downloaded from https://scijournals.onlinelibrary.wiley.com/doi/10.1002/esc3.1729 by Cochrane France, Wiley Online Library on [05/06/2025]. See the Terms and Conditions (https://onlinelibrary.wiley.com/terms-and-conditions) on Wiley Online Library for rules of use; OA articles are governed by the applicable Creative Commons License

when there is an obvious thermal boundary layer flow reaching stable state. Figure 12 shows the correlation between $\theta/(\Gamma/\kappa)^{2/5}$ and $Bo^{-1/5}$ at different points under different cases in steady-state. As expected, the fit results at different points all follow a linear relationship.

4 | ANALYSIS OF AIR CHANGES PER HOUR AND HEAT EXCHANGE PERFORMANCE

Solar chimneys are a technology that harnesses solar energy to improve natural ventilation. It is necessary to apply the energy saving and environmental protection methods of solar chimneys to practical engineering. Therefore, ventilation frequency and air exchange are introduced in this study to investigate the suitability of solar chimneys in practical projects.

The number of air changes is a commonly used indicator for measuring the supply air volume in air conditioning engineering, and is an important indicator for evaluating the performance of solar chimneys.[43–45] Its definition is as follows[46]:

$$n = \frac{G}{V_{\text{room}}}, \tag{50}$$

where n is the ventilation rate; G is the ventilation quantity, $G = 3600\, m/\rho$; V_{room} is the volume of room.

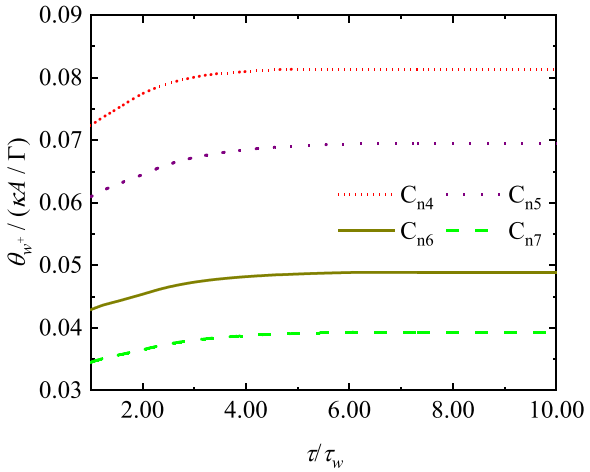


FIGURE 10 Temperature scale before the flow reaches steady state in cases without distinct thermal boundary layer: $\theta_{w+}/(\kappa A/\Gamma)$ and τ/τ_w.

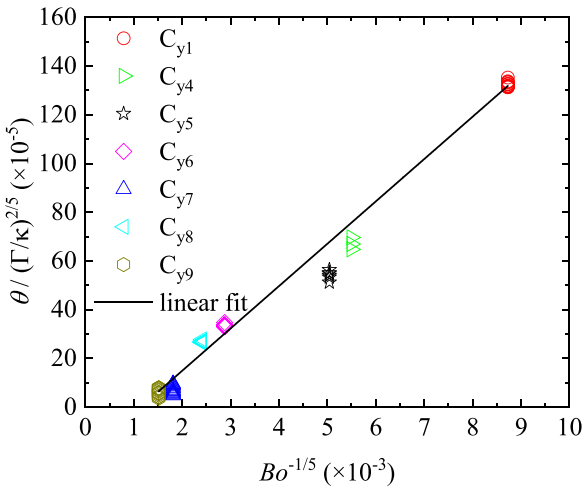


FIGURE 12 The temperature scale with distinct thermal boundary layer in steady-sate.

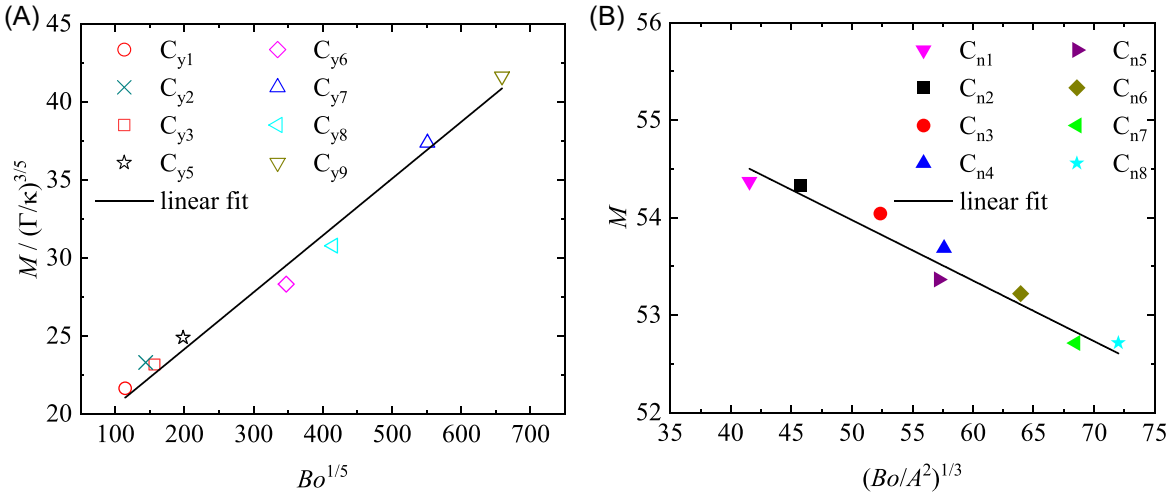


FIGURE 11 The mass flow rate scale verification of boundary layer near absorb wall in steady-sate. (A) Steady-state mass rate of flow scale with distinct thermal boundary layer: $M/(\Gamma/\kappa)^{3/5}$ and $Bo^{-1/5}$. (B) Steady-state mass rate of flow scale without distinct thermal boundary layer: M and $(Bo/A)^{1/3}$.

20500505, 2024, 5, Downloaded from https://scijournals.onlinelibrary.wiley.com/doi/10.1002/ese3.1729 by Cochrane France, Wiley Online Library on [05/06/2025]. See the Terms and Conditions (https://onlinelibrary.wiley.com/terms-and-conditions) on Wiley Online Library for rules of use; OA articles are governed by the applicable Creative Commons License

According to the mass flow rate scales (24) and (41) of the full development stage of the two boundary flow regimes. Ventilation volume G in the air change per hour formula can be expressed on the following scale:

$$G \sim 3600\kappa \mathrm{M}, \tag{51}$$

Then the air change per hour n is:

$$n \sim \frac{3600\kappa \mathrm{M}}{V_{\mathrm{room}}}. \tag{52}$$

Taking the solar chimney with $A = 7.5$ calculated in this paper as an example, it is assumed that the length × width × height of the room is 4.0 m × 4.5 m × 3.0 m when it is applied to a residence. According to the atmospheric meteorological parameters of Shijiazhuang City, Hebei Province, China, the air density is 1.205 kg/m^3. Shijiazhuang is a cold winter and hot summer area with four distinct seasons. Spring and autumn are transitional seasons, suitable for natural ventilation by a solar chimney. The number of air changes is approximately:

$$n = \frac{3600\kappa \times (21.96 \sim 25.26)}{4.0 \times 4.5 \times 3.0} = 8.58 \sim 9.87 \text{ (times/h)}.$$

When the solar chimney is applied to the underground garage. Take two standard parking spaces in the underground garage, with a size of 4.8 m × 2.0 m × 1.8 m, and a height of 3.0 m, then the air changes times are approximately:

$$n = \frac{3600\kappa \times (21.96 \sim 25.26)}{2 \times 4.8 \times 2.0 \times 1.8} = 8.05 \sim 9.25 \text{ (times/h)}.$$

Article 4.2 of the Indoor Air Quality Standard[47] and Article 3.1.9 of the Design Code for Heating, Ventilation, and Air Conditioning[48] stipulate that for residential buildings, the minimum fresh air volume required by indoor personnel should be greater than or equal to 30 m^3/h, that is, the minimum number of ventilation and air changes per person per hour is 0.56 times/h. Article 8.1.5 of the Code for Fire Protection Design of Garages, Repair Garages and Parking Lots[49] stipulates that the number of ventilation changes per hour is six to eight times.

Comparing the number of ventilation changes obtained in this study with the requirements in codes and standards, it is found that the ventilation capabilities of this solar chimney can meet the comfort and health requirements of residential buildings and underground garages in the code.[47–49]

It is evident from the scale analysis results and the air changes per hour that chimney width, height, and Ra are the primary parameters influencing chimney ventilation. Flow conditions at $Ra > A^5\Gamma^2/\mathrm{Pr}\kappa^2$ are more suitable for ventilation applications. In the range studied in this paper, C_{y9} ($H = 15.0$, $l/H = 0.2$, $A = 75.0$, $Ra = 1.75 \times 10^{14}$) has the best ventilation performance.

An essential metric for assessing the heat exchange capabilities of a solar chimney is heat exchange efficiency.[50,51] It represents the ability of a solar chimney to convert solar energy into usable heat, thereby removing indoor heat. The following formulas can be used to compute the heat released by natural ventilation[52]:

$$Q_{\mathrm{out}} = Q_0 - V_{\mathrm{room}} C_v (T - T_0), \tag{53}$$

where Q_{out} is the natural ventilation heat dissipation (J); C_v is the constant specific heat capacity (J/(kg·K)); T is the steady-state outlet temperature (K); T_0 is the initial temperature (K); Q_0 is the heat absorbed by the absorbing wall (J), $Q_0 = 3\ 600q(H + L)$.

In the above equation, $Q_0 = 3600q(H + L)$. The heat exchange efficiency is:

$$\eta = \frac{Q_{out}}{Q_0} \times 100\%. \tag{54}$$

As well as the number of air changes per hour, when the combined solar chimney with $A = 7.5$ is applied to residential and parking lots, the heat exchange efficiency ranges from 63.33% to 98.44%.

5 | CONCLUSION

This research uses dimensional analysis to investigate the flow and heat transfer control mechanism of transient natural convection in a combined solar chimney with a fixed heat flux on the absorbing wall. Numerical simulation results are provided to verify the scaling relations.

There may be two flow regimes depending on Ra for a solar chimney that presents a fixed heat flux to the absorption wall. For $Ra > A^5\Gamma^2/\mathrm{Pr}\kappa^2$, the flow with obvious thermal boundary layer is formed under the strong convection. Some new scale relationships for this flow state are obtained through scaling analysis, including temperature, vertical velocity, mass flow and characteristic time scales in the thermal boundary layer. For example, the characteristic time scale for reaching the full development stage is expressed by $t_s \sim H^2/Bo^{2/5}\kappa^{4/5}\Gamma^{1/5}$,

20500505, 2024, 5, Downloaded from https://scijournals.onlinelibrary.wiley.com/doi/10.1002/ese3.1729 by Cochrane France, Wiley Online Library on [05/06/2025]. See the Terms and Conditions (https://onlinelibrary.wiley.com/terms-and-conditions) on Wiley Online Library for rules of use; OA articles are governed by the applicable Creative Commons License

and the thermal boundary layer thickness in the fully developed stage is expressed by $\delta_{T,s} \sim H\Gamma^{2/5}/Bo^{1/5}\kappa^{2/5}$. This flow state is more suitable for ventilation applications.

For $Ra < A^5\Gamma^2/\mathrm{Pr}\kappa^2$, a flow pattern without an obvious thermal boundary layer is generated. Several new scaling relations are obtained by scaling analysis, including temperature, vertical velocity, mass flow, and characteristic time in the thermal boundary layer. For example, the mass flow scale is expressed by $m \sim \rho\kappa Bo^{1/3}/A^{2/3}$. For both flow regimes, the ventilation properties strongly depend on Ra.

Finally, the ventilation and heat exchange properties of the chimney are analyzed. It is of theoretical interest to apply the solar chimney with aspect ratio $A = 7.5$ to practical engineering, which can fulfill the ventilation requirements of an ordinary residential house with two standard parking spaces and an underground garage.

6 | LIMITATIONS, IMPROVEMENTS AND FUTURE DIRECTION

This study simplifies the physical model in terms of dimension and boundary conditions, ignoring the development of flow heat transfer in spanwise space and the change of the external environment with time. As a result, there are some temporal and spatial limitations on the outcomes of theoretical analysis and numerical simulation. In future studies, 3D physical models that are closer to actual engineering can be considered, and more complex environmental conditions can be considered; such as the variations in medium temperature and thermal radiation conditions throughout time. Further, we will consider numerical and experimental studies that are closer to engineering reality.

NOMENCLATURE

A	solar chimney aspect ratio
Bo	Boussinesq number
c_p	specific heat capacity ($\mathrm{J\cdot kg^{-1}\cdot K^{-1}}$)
g	gravitational acceleration ($\mathrm{m\cdot s^{-2}}$)
G	ventilation quantity (kg)
H	vertical chimney length (m)
k	thermal conductivity coefficient ($\mathrm{W\cdot m^{-1}\cdot K^{-1}}$)
l	length of inclined section of chimney (m)
m	air mass flow rate in steady state ($\mathrm{kg\cdot s^{-1}}$)
M	dimensionless air mass flow rate in steady state
n	ventilation rate ($\mathrm{times\cdot h^{-1}}$)
Nu	Nusselt number
p	pressure (Pa)
P	dimensionless pressure
Pr	Prandtl number
q	heat flux of absorbing wall ($\mathrm{W\cdot m^{-2}}$)
Q_0	energy rate absorbed by the absorbing wall (J)
Q_{out}	energy rate removed by natural ventilation (J)
Ra	Rayleigh number
t_f	time scaling of heat conduction and convective equilibrium in the absence of an obvious thermal boundary layer (s)
t_s	time scaling of heat conduction and convective equilibrium with an obvious thermal boundary layer (s)
t_w	time scaling at thermal boundary layer thickness reaches the width of the chimney without obvious thermal boundary layer flow regime (s)
T_0	initial temperature (K)
u,v	dimensional velocity in the x and y directions ($\mathrm{m\cdot s^{-1}}$)
U,V	dimensionless velocity in the X and Y directions
v_T	thermal boundary layer velocity scaling for nonstationary terms and buoyancy equilibria with an obvious thermal boundary layer ($\mathrm{m\cdot s^{-1}}$)
$v_{T,f}$	thermal boundary layer velocity scaling for heat conduction and convective equilibrium in the absence of an obvious thermal boundary layer ($\mathrm{m\cdot s^{-1}}$)
$v_{T,s}$	thermal boundary layer velocity scaling for convection and heat conduction equilibrium with an obvious thermal boundary layer ($\mathrm{m\cdot s^{-1}}$)
$v_{T,w}$	velocity scaling of the thermal boundary layer thickness up to the chimney width in the absence of an obvious thermal boundary layer flow regime ($\mathrm{m\cdot s^{-1}}$)
V_T	dimensionless velocity scaling
W	solar chimney width (m)
x、y	dimensional coordinates
X、Y	nondimensional coordinate
β	thermal expansion coefficient ($1\cdot\mathrm{K^{-1}}$)
δ_T	thermal boundary layer thickness (m)
δ_T,s	thermal boundary layer thickness with an obvious thermal boundary layer heat conduction and convective equilibrium (m)
δvi	inner velocity boundary layer thickness of obvious thermal boundary layer (m)
$\delta_{vi,s}$	steady inner velocity boundary layer thickness with an obvious thermal boundary layer (m)
$\delta_{vo,s}$	steady outer velocity boundary layer thickness with an obvious thermal boundary layer (m)
ΔT	temperature difference (K)
ΔT_w	temperature difference when the thickness of the thermal boundary layer reaches the width of the chimney without an obvious thermal boundary layer (K)

20500505, 2024, 5, Downloaded from https://scijournals.onlinelibrary.wiley.com/doi/10.1002/ese3.1729 by Cochrane France, Wiley Online Library on [05/06/2025]. See the Terms and Conditions (https://onlinelibrary.wiley.com/terms-and-conditions) on Wiley Online Library for rules of use; OA articles are governed by the applicable Creative Commons License

ΔT_w^+ temperature difference after thermal boundary layer thickness reaches the width of the chimney without an obvious thermal boundary layer (K)

$\Delta T_{w,f}^+$ temperature difference of heat conduction and convection equilibrium without an obvious thermal boundary layer (K)

κ thermal diffusion coefficient ($m^2 \cdot s^{-1}$)

ν kinematic viscosity coefficient ($m^2 \cdot s^{-1}$)

ν_t turbulence viscosity coefficient ($m^2 \cdot s^{-1}$)

ν' sum of turbulent and laminar viscosity coefficients ($m^2 \cdot s^{-1}$)

ρ air density ($kg \cdot m^{-3}$)

τ dimensionless time

τ_s dimensionless time scaling of heat conduction and convective equilibrium with an obvious thermal boundary layer

τ_w dimensionless time scaling at thermal boundary layer thickness reaches the width of the chimney without obvious thermal boundary layer flow regime

θ dimensionless temperature

Γ generalized diffusion coefficient

AUTHOR CONTRIBUTIONS

Huimin Cui: Methodology, conceptualization, supervision, writing-review and editing. **Mengjiao Han**: Data curation, writing-original draft, writing-review and editing. **Jitao Zhang**: Writing-review and editing. **Zhiming Han**: Supervision, writing-review and editing. **Feng Xu**: Supervision, writing-review and editing. **Qingkuan Liu**: Writing-review and editing.

ACKNOWLEDGMENTS

The study is financially supported by Natural Science Foundation of Hebei Province (E2022210069), Natural Science Foundation of Hebei Province Innovative Research Group Project (E2022210078), National Natural Science Foundation of China (11802186), and Central Leading Local Science and Technology Development Fund Project (236Z5410G); High Talents Project of Hebei Province (Hebei Office [2019] No. 63).

CONFLICT OF INTEREST STATEMENT

The authors declare no conflict of interest.

DATA AVAILABILITY STATEMENT

Data will be made available on request.

ORCID

Huimin Cui http://orcid.org/0009-0006-5884-3985

REFERENCES

1. Tang M. Effect of ventilation size on natural ventilation of solar chimney. *Low Temp Arch Technol*. 2018;40(5):165-168. doi:10.13905/j.cnki.dwjz.2018.03.041
2. Miyazaki T, Akisawa A, Kashiwagi T. The effects of solar chimneys on thermal load mitigation of office buildings under the Japanese climate. *Renew Energy*. 2006;31(7):987-1010. doi:10.1016/j.renene.2005.05.003
3. Zhang L, Dong Z, Liu F, et al. Analysis of solar chimney application for building heating and cooling in different climates in China. *J Energy Eng*. 2023;149(1):04022060. doi:10.1061/JLEED9.EYENG-4612
4. Patterson J, Imberger J. Unsteady natural convection in a rectangular cavity. *J Fluid Mech*. 1980;100(1):65-86. doi:10.1017/S0022112080001012
5. Poulikakos D, Bejan A. The fluid dynamics of an attic space. *J Fluid Mech*. 1983;131:251-269. doi:10.1017/S0022112083001317
6. Cui H, Xu F, Saha SC. A three-dimensional simulation of transient natural convection in a triangular cavity. *Int J Heat Mass Transfer*. 2015;85:1012-1022. doi:10.1016/j.ijheatmasstransfer.2015.02.055
7. Lei C, Patterson JC. Unsteady natural convection in a triangular enclosure induced by absorption of radiation. *J Fluid Mech*. 2002;460:181-209. doi:10.1017/S0022112002008091
8. Lin W, Armfield SW, Patterson JC, Lei C. Prandtl number scaling of unsteady natural convection boundary layers for Pr>1 fluids under isothermal heating. *Phys Rev E*. 2009;79(6):066313. doi:10.1103/PhysRevE.79.066313
9. Zhai H, Nie B, Chen B, Xu F. Unsteady flows on a roof imposed by a periodic heat flux: 2D simulation and scaling analysis. *Int J Therm Sci*. 2019;145:106002. doi:10.1016/j.ijthermalsci.2019.106002
10. Saha SC. Scaling of free convection heat transfer in a triangular cavity for $Pr > 1$. *Energy Build*. 2011;43(10):2908-2917. doi:10.1016/j.enbuild.2011.07.016
11. Saha SC, Patterson JC, Lei C. Natural convection boundary-layer adjacent to an inclined flat plate subject to sudden and ramp heating. *Int J Therm Sci*. 2010;49(9):1600-1612. doi:10.1016/j.ijthermalsci.2010.03.017
12. He Y. *Scaling Analysis and Direct Numerical Simulation Study on Temperature Field and Velocity Field in Solar Chimney*. MA English Dissertation. School of Energy Environmental Science, Yunnan Normal University, Kunming, China, 2007.
13. Khanal R, Lei C. A scaling investigation of the laminar convective flow in a solar chimney for natural ventilation. *Int J Heat Fluid Flow*. 2014;45:98-108. doi:10.1016/j.ijheatfluidflow.2013.11.002
14. Chen ZD, Bandopadhayay P, Halldorsson J, Byrjalsen C, Heiselberg P, Li Y. An experimental investigation of a solar chimney model with uniform wall heat flux. *Build Environ*. 2003;38(7):893-906. doi:10.1016/S0360-1323(03)00057-X
15. Li A, Hao C, Zhang H. Experimental study on solar chimney for natural ventilation. *Acta Energiae Sol Sin*. 2009;30(4):460-464. doi:10.3321/j.issn:0254-0096.2009.04.011
16. Lei F, Su Y, Xu X. Numerical modeling of effect of channel width on heat transfer and ventilation in a built-in PV-Trombe wall. *Acta Energiae Sol Sin*. 2015;36(7):1710-1716. doi:10.3969/j.issn.0254-0096.2015.07.028

20500505, 2024, 5, Downloaded from https://scijournals.onlinelibrary.wiley.com/doi/10.1002/esc3.1729 by Cochrane France, Wiley Online Library on [05/06/2025]. See the Terms and Conditions (https://onlinelibrary.wiley.com/terms-and-conditions) on Wiley Online Library for rules of use; OA articles are governed by the applicable Creative Commons License

17. Su Y, Xu X, Deng W. Numerical study of thermal performance in cell built-in PV-Trombe wall. *Acta Energiae Sol Sin*. 2016;37(10):2639-3646. doi:10.3969/j.issn.0254-0096.2016.10.028
18. Imran AA, Jalil JM, Ahmed ST. Induced flow for ventilation and cooling by a solar chimney. *Renew Energy*. 2015;78:236-244. doi:10.1016/j.renene.2015.01.019
19. Khedari J, Hirunlabh J, Bunnag T. Experimental study of a roof solar collector towards the natural ventilation of new house. *Energy Build*. 1997;26(2):159-164. doi:10.1016/S0378-7788(96)01030-4
20. Zhao P. Numerical study of enhanced stack ventilation of solar energy chimney. *J Xi'an Inst Technol*. 2004;24(2):181-184. doi:10.3969/j.issn.1673-9965.2004.02.020
21. Bassiouny R, Koura NSA. An analytical and numerical study of solar chimney use for room natural ventilation. *Energy Build*. 2008;40(5):865-873. doi:10.1016/j.enbuild.2007.06.005
22. Xue Y, Su Y. Numerical study on impacts of solar chimney structure on ventilation effects. *HVAC*. 2011;40(10):79-83. doi:10.3969/j.issn.1002-8501.2011.10.021
23. Burek SAM, Habeb A. Air flow and thermal efficiency characteristics in solar chimneys and trombe walls. *Energy Build*. 2007;39(2):128-135. doi:10.1016/j.enbuild.2006.04.015
24. Yang Q, Du W, Zhang J. Research on ventilation performance of a series solar chimney integrated with a building. *Acta Energiae Sol Sin*. 2010;31(7):873-878. doi:10.19912/j.0254-0096.2010.07.016
25. Duan S. *Numerical Investigation on Ventilation Characteristics and Optimization of Combined Solar Chimney*. MA English Dissertation. College of Environmental Science and Engineering, Taiyuan University Technology, Taiyuan, China, 2015.
26. Mandal DK, Biswas N, Manna NK, Gayen DK, Benim AC. An application of artificial neural network (ANN) for comparative performance assessment of solar chimney (SC) plant for green energy production. *Sci Rep*. 2024;14(1):979. doi:10.1038/s41598-023-46505-1
27. Biswas N, Mandal DK, Bose S, Manna NK, Benim AC. Experimental treatment of solar chimney power plant—a comprehensive review. *Energies*. 2023;16(17):6134. doi:10.3390/en16176134
28. Kumar Mandal D, Biswas N, Manna NK, Benim AC. Impact of chimney divergence and sloped absorber on energy efficacy of a solar chimney power plant (SCPP). *Ain Shams Eng J*. 2024;15(2):102390. doi:10.1016/j.asej.2023.102390
29. Biswas N, Kumar Mandal D, Manna NK, Cemal Benim A. Novel stair-shaped ground absorber for performance enhancement of solar chimney power plant. *Appl Therm Eng*. 2023;227:120466. doi:10.1016/j.applthermaleng.2023.120466
30. Mandal DK, Biswas N, Barman A, Chakraborty R, Manna NK. A novel design of absorber surface of solar chimney power plant (SCPP): thermal assessment, exergy and regression analysis. *Sustain Energy Techn*. 2023;56:103039. doi:10.1016/j.seta.2023.103039
31. Mandal DK, Pradhan S, Chakraborty R, Barman A, Biswas N. Experimental investigation of a solar chimney power plant and its numerical verification of thermo-physical flow parameters for performance enhancement. *Sustain Energy Tech*. 2022;50:101786. doi:10.1016/j.seta.2021.101786
32. Zha X, Qin M. Experimental investigations and numerical analysis of solar chimney for building ventilation. *Building Sci*. 2017;33(4):8-14. doi:10.13614/j.cnki.11-1962/tu.2017.04.02
33. Ren XH, Liu RZ, Wang YH, Wang L, Zhao FY. Thermal driven natural convective flows inside the solar chimney flush-mounted with discrete heating sources: reversal and cooperative flow dynamics. *Renew Energy*. 2019;138:354-367. doi:10.1016/j.renene.2019.01.090
34. Nouanégué HF, Alandji LR, Bilgen E. Numerical study of solar-wind tower systems for ventilation of dwellings. *Renew Energy*. 2008;33(3):434-443. doi:10.1016/j.renene.2007.03.001
35. Lei X. *The application of solar chimney for strengthening natural ventilation in multistoried building*. MA English Dissertation. School of Energy Science and Engineering, Central South University, Changsha, China, 2011.
36. Bejan A. *Convection Heat Transfer*. 3rd ed. JWS; 2004.
37. Lin W, Armfield SW. Unsteady natural convection on an evenly heated vertical plate for Prandtl number $Pr < 1$. *Phys Rev E: Stat Nonlin Soft Matter Phys*. 2005;72(6):066309. doi:10.1103/PhysRevE.72.066309
38. Gong J, Chew LW, Lee PS. Shape optimization of high-rise solar chimneys to improve the uniformity of flowrate distribution. *Build Environ*. 2023;243:110650. doi:10.1016/j.buildenv.2023.110650
39. Pasut W, De Carli M. Evaluation of various CFD modelling strategies in predicting airflow and temperature in a naturally ventilated double skin façade. *Appl Therm Eng*. 2012;37:267-274. doi:10.1016/j.applthermaleng.2011.11.028
40. Zamora B, Kaiser AS. 3D effects in numerical simulations of convective flows in cubical open cavities. *Int J Therm Sci*. 2014;77:172-185. doi:10.1016/j.ijthermalsci.2013.11.004
41. Wang F. *Computational Fluid Dynamics Analysis—Principles and Applications of CFD Software*. Tsinghua University Press; 2004:124-125.
42. Yan H, Zhang HY. Comparison of different radiation models for numerical simulation of solar radiation. *En Consv Tech*. 2015;33(5):428-431. doi:10.3969/j.issn.1002-6339.2015.05.009
43. Jiménez-Xamán C, Xamán J, Moraga NO, et al. Solar chimneys with a phase change material for buildings: an overview using CFD and global energy balance. *Energy Build*. 2019;186(1):384-404. doi:10.1016/j.enbuild.2019.01.014
44. Villar-Ramos MM, Macias-Melo EV, Aguilar-Castro KM, et al. Parametric analysis of the thermal behavior of a single-channel solar chimney. *Sol Energy*. 2020;209:602-617. doi:10.1016/j.solener.2020.08.072
45. Moosavi L, Zandi M, Bidi M, Behroozizade E, Kazemi I. New design for solar chimney with integrated windcatcher for space cooling and ventilation. *Build Environ*. 2020;181(15):106785. doi:10.1016/j.buildenv.2020.106785
46. Bojić M, Johannes K, Kuznik F. Optimizing energy and environmental performance of passive Trombe wall. *Energy Build*. 2014;70:279-286. doi:10.1016/j.enbuild.2013.11.062
47. GB/T 18883-2002. *Indoor Air Quality Standard*. Standards Press of China. 2009.
48. GB 50019-2003. *Code for Design of Heating Ventilation and Air Conditioning*. China Planning Press. 2015.
49. GB 50067-2014. *Code for Fire Protection Design of Garage, Motor Repair Shop and Parking Area*. Standards Press of China, 2021.
50. Duan S, Jing C, Zhao Z. Energy and exergy analysis of different Trombe walls. *Energy Build*. 2016;126:517-523. doi:10.1016/j.enbuild.2016.04.052

20500505, 2024, 5, Downloaded from https://scijournals.onlinelibrary.wiley.com/doi/10.1002/ese3.1729 by Cochrane France, Wiley Online Library on [05/06/2025]. See the Terms and Conditions (https://onlinelibrary.wiley.com/terms-and-conditions) on Wiley Online Library for rules of use; OA articles are governed by the applicable Creative Commons License

51. Yu B, Li N, Xie H, Ji J. The performance analysis on a novel purification-cleaning Trombe wall based on solar thermal sterilization and thermal catalytic principles. *Energy*. 2021;225:120275. doi:10.1016/j.energy.2021.120275
52. Qin YX. An approximate calculating method for the heat discharge capacity of natural ventilation. *Ind Saf Dust Control*. 1999;6:24-25.

How to cite this article: Cui H, Han M, Zhang J, Han Z, Xu F, Liu Q. Theoretical analysis and numerical study of natural convection inside combined solar chimney. *Energy Sci Eng*. 2024;12:2052-2071. doi:10.1002/ese3.1729

20500505, 2024, 5, Downloaded from https://scijournals.onlinelibrary.wiley.com/doi/10.1002/ese3.1729 by Cochrane France, Wiley Online Library on [05/06/2025]. See the Terms and Conditions (https://onlinelibrary.wiley.com/terms-and-conditions) on Wiley Online Library for rules of use; OA articles are governed by the applicable Creative Commons License